ACS APPLIED MATERIALS & INTERFACES

www.acsami.org

Research Article

Intrinsic and Extrinsic Tunability of Double-Network Hydrogel Strength and Lubricity

Ming Jun Lee and Rosa M. Espinosa-Marzal*

Cite This: *ACS Appl. Mater. Interfaces* 2023, 15, 20495−20507

Read Online

ACCESS | Metrics & More | Article Recommendations | Supporting Information

ABSTRACT: Double-network (DN) hydrogels are promising materials for tissue engineering due to their biocompatibility, high strength, and toughness, but understanding of their microstructure−property relationships still remains limited. This work investigates a DN hydrogel comprising a physically crosslinked agarose, as the first network, and a chemically crosslinked copolymer with a varying ratio of acrylamide and acrylic acid, as the second network. The charge, intrinsic to most DN hydrogels, introduces a responsive behavior to chemical and electrical stimuli. The DN strengthens agarose hydrogels, but the strengthening decreases with the swelling ratio resulting from increasing acrylic acid content or reducing salt concentration. Through careful imaging by atomic force microscopy, the heterogenous surface structure and properties arising from the DN are resolved, while the lubrication mechanisms are elucidated by studying the heterogeneous frictional response to extrinsic stimuli. This method reveals the action of the first (agarose) network (forming grain boundaries), copolymer-rich and poor regions (in grains), charge and swelling in providing lubrication. Friction arises from the shear of the polymeric network, whereas hydrodynamic lift and viscoelastic deformation become more significant at higher sliding velocities. We identify the copolymer-rich phase as the main source of the stimulus-responsive behavior. Salt concentration enhances effective charge density and reduces viscoelastic deformation, while electric bias swells the gel and improves lubrication. This work also demonstrates the dynamic control of interfacial properties like hydrogel friction and adhesion, which has implications for other areas of study like soft robotics and tissue replacements.

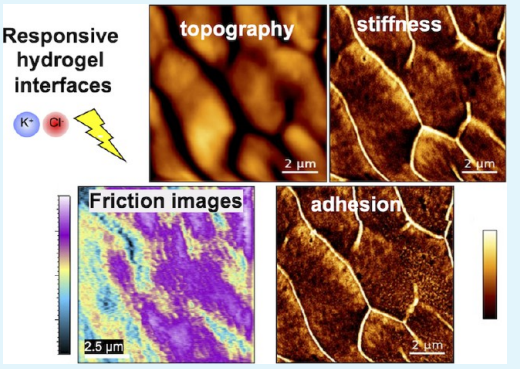

KEYWORDS: *hydrogel, friction, lubrication, microstructure, double network, friction force microscopy, responsive interface*

1. INTRODUCTION

Hydrogels are versatile soft materials that have been thoroughly investigated as replacement for biological tissues such as cartilage,[1−5] as well as for soft robotics and actuator applications.[6−8] Their microstructural resemblance to soft tissue, biocompatibility, and potential tunability of surface and bulk properties are key advantages that advent this field of research. However, conventional single-network (SN) hydrogels are relatively weak and brittle with several orders of magnitude lower fracture toughness than human tissues, including cartilage.[9,10] Thus, there is a need for the design of mechanically stronger hydrogels, while possessing tunable surface and bulk properties for in situ or ex situ control. Double-network (DN) hydrogels are one potential solution to this problem as they generally have stronger mechanical strength than SN hydrogels.[11,12] Furthermore, the presence of intrinsic charge introduces the possibility of responsive behavior to external stimuli[13,14] as well as high lubricity.[15,16]

DN hydrogels were pioneered in 2003 by Gong. A key design principle was the selection of a polyelectrolyte (poly(2-acrylamido-2-methylpropane sulfonic acid, PAMPS) as the first network, and a neutral, loosely crosslinked polymer (poly(*N*,*N*′-dimethyl acrylamide, PDMAAm), as the second network. This hydrogel exhibits impressive fracture stress and strain (17 MPa and 92%, respectively), along with moderately low friction coefficients ($\mu \sim 10^{-2}$ to 10^{-1}). High lubricity ($\mu \sim 10^{-5}$) could only be achieved if a linear, free to diffuse, polymer was added to the hydrogel.[12] Several mechanisms like sacrificial fracture, chain pull-out, and connected energy dissipation across entangled chains have been proposed to explain mechanical strength.[11,12,17,18] Several mechanisms like sacrificial fracture, chain pull-out, and connected energy dissipation across entangled chains have been elaborated to explain mechanical strength.[11,17,18] Building on Gong's pioneering work, many researchers have engineered DN hydrogels that are mechanically strong and self-healing.[19,20] DN hydrogels with tensile modulus up to ∼2000 kPa and fracture strains up to

Received: January 20, 2023
Accepted: March 31, 2023
Published: April 13, 2023

Table 1. Quantities of Chemicals Used in the Preparation of SN and DN Hydrogels in 10 mL Solution of Agarose, Acrylamide, and Acrylic Acid

sample	DI water (mL)	acrylamide 40% solution (mL)	methylene bisacrylamide 2% solution (mL)	acrylic acid 99% (mL)	5 M NaOH (mL)	initiator solution (mL)
3Ag	10					
3AgP(Am-co-AAc) 6:4	5.857	2.10	1.51	0.533	0.5	0.175
3AgP(Am-co-AAc) 7:3	5.638	2.45	1.51	0.400	0.5	0.175
3AgP(Am-co-AAc) 8:2	5.419	2.8	1.51	0.266	0.3	0.175

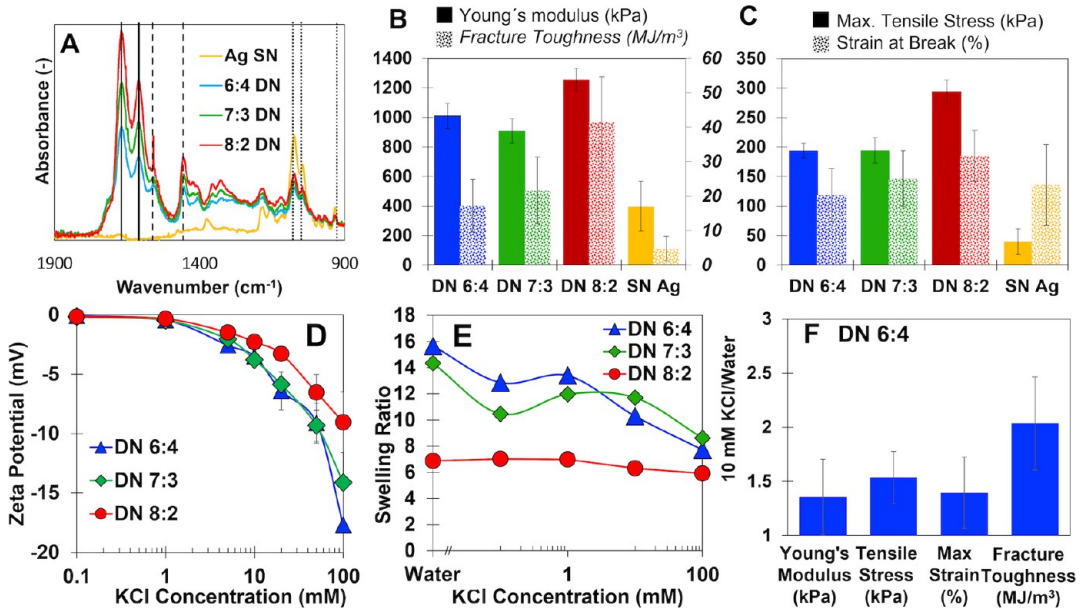

Figure 1. DN formation and strengthening. (A) FTIR spectroscopy (absorbance) of 3Ag SN hydrogel compared to 3AgP(Am-co-AAc) 6:4, 7:3, and 8:2 DN hydrogels showing the presence of functional groups to confirm successful synthesis of hydrogels. (B and C) Mechanical properties of SN and DN hydrogels. All hydrogels were equilibrated in DI water. (D) Zeta potential and (E) swelling ratio at varying KCl concentration. The swelling ratio was calculated by dividing the equilibrated weight of the hydrogel by its dried weight. The pH of the solutions is 6.1, 6.08, 5.65, 5.65, 5.58, 5.56, 5.53, and 5.42 for DI water and 0.1, 1, 5, 10, 20, 50, and 100 mM KCl, respectively. For agarose SN hydrogels, the zeta potential is −2.04, −5.29, −4.15, and −6.15 mV, while the swelling ratio is 31.2, 31.8, 31.9, and 27.0 at 0.1, 1, 10, and 100 mM KCl, respectively. The swelling ratio of SN hydrogels in water is 33. (F) Ratio between the mechanical properties of the DN 6:4 hydrogels equilibrated in 10 mM KCl and in water for 24 h, respectively.

~5000% have been already engineered. For a comprehensive review of the synthesis methods of DN hydrogels as well as their mechanical properties, we refer the readers to ref 20.

The surface microstructure plays an important role in DN hydrogel lubrication but needs further investigation to understand the underlying mechanisms.[21] Zhang et al. revealed that the combination of a crosslinking density gradient and swelling ratio mismatch led to a highly lubricious hydrogel sub-surface. By exploiting environmental oxygen "contamination", the synthesis setup partially inhibited free-radical polymerization of PAMPS in the near-surface region of PAMPS-alginate DN hydrogels. After removing the delaminated top surface, its sub-surface exhibited a friction coefficient of 0.02 in gel-on-glass.[22] Shoaib et al.[23] investigated the microstructure−property relationship of agarose-polyacrylamide DN hydrogels. Mechanical strengthening of the DN hydrogel over its individual components required a delicate balance between monomer concentration and crosslinking density. Friction properties displayed a composition dependence; specifically, they were shown to depend on the network enriched at the surface. Interestingly, the frictional characteristics were convoluted by a binary response arising from the solvent viscosity and the polymer network at the surface. The heterogeneous surface structure originating from the DN seemed to spatially influence friction as well.[23] This finding calls for a characterization method of the frictional response of heterogeneous DNs.

This work investigates a series of agarose/poly(acrylamide-co-acrylic acid) DN hydrogels with a varying acrylamide to acrylic acid ratio. To the best of the authors' knowledge, there is only one reported study of this system by Peng et al.,[14] which studied the shape recovery of these gels mediated by the photoreduction of Fe(III) to Fe(II) in the presence of citric acid as a reducing agent. Here, we first present mechanical, zeta potential, and swelling measurements to understand the strengthening mechanism of the DN. Atomic and lateral force microscopy is used to visualize the heterogeneous surface topography, frictional and adhesive characteristics of the hydrogel, and the effect of salt concentration on these properties. The connection between surface images, load- and velocity-dependent friction images, charge density, and swelling ratio reveals the underlying lubrication mechanisms. This is a novel approach that allows relating the hydrogel microstructure to a frictional response. In a proof-of-concept experiment, we demonstrate that charged DN hydrogels provide a means to dynamically control surface topography, stiffness, adhesion, and friction via an electric potential. To the best of our knowledge, this is the first study of the interfacial properties of this DN system and of its responsive interface.

https://doi.org/10.1021/acsami.3c00949
ACS Appl. Mater. Interfaces 2023, 15, 20495−20507

2. RESULTS AND DISCUSSION

Agarose/poly(acrylamide-co-acrylic acid) DN hydrogels were prepared via a two-step polymerization process that involves the thermal transition of agarose first followed by UV-initiated radical polymerization of acrylamide-co-acrylic acid. The choice to include the charge in the second network is due to the need to reduce the duration of the exposure of the acrylamide and acrylic acid solutions to high temperatures; see details in the Materials and Methods section. Throughout this study, all the hydrogels were synthesized with 3 wt % agarose and 13.8 wt % copolymer. The copolymer was designed with various mole ratios between acrylamide (Am) and acrylic acid (AAc), with the crosslinker bis-acrylamide (bis-Am) at constant 1 mol % with respect to the total monomer molar content. Specific quantities pertaining to the synthesis of hydrogels are detailed in Table 1. The nomenclature used is as follows: 3Ag refers to 3 wt % agarose SN hydrogel; 3AgP(Am-co-AAc) refers to the DN hydrogel composed of 3 wt % agarose and 13.8 wt % copolymer. The ratios 6:4, 7:3, and 8:2 refer to the mole ratios between Am and AAc in the copolymer.

FTIR was used to identify the functional groups of each monomer. The IR spectra of agarose SN (3Ag) and 3AgP(Am-co-AAc) 6:4, 7:3, and 8:2 DN hydrogels are overlayed in Figure 1A for comparison. Absorbance peaks at 931, 1048, and 1080 cm^{-1} correspond to 3,6-anhydrogalactose, C−O bending, and C−H bending of agarose, respectively. These peaks are observed in SN and DN hydrogels, thus proving the successful incorporation of agarose into all three DN hydrogels. As for the copolymer component within the DN hydrogel, absorbance peaks at 1599 and 1672 cm^{-1} correspond to known amide II and amide I groups of acrylamides, respectively, while peaks at 1458 and 1565 cm^{-1} correspond to acrylic and COO^- groups of acrylic acid, respectively. Note that the acrylic acid is partially deprotonated due to the pH adjustment to 5 during synthesis (pH > pK_a = 4.2).[24] IR results demonstrate the successful synthesis of the DN hydrogels.

2.1. DN Strengthens Agarose Hydrogels and Strengthening Increases with the Decreasing Swelling Ratio. The mechanical properties of reference SN hydrogels and DN hydrogels were determined from tensile tests; details of the setup can be found in Experimental Methods. Copolymer SN hydrogels were too soft and weak to be tested, and hence, only agarose SN hydrogels were taken as reference. Young's Modulus, fracture stress, fracture strain, and fracture toughness were extracted from the resulting stress−strain curves for at least four hydrogels each; representative curves are shown in Figure S1. Stress−strain curves indicate brittle fracture without necking; thus, fracture stress and ultimate tensile stress are equivalent, and the fracture surface is flat. The brittle fracture is also characteristic of agarose SN hydrogels (Figure S2). Young's modulus, fracture toughness, and fracture stress of all DN hydrogels (6:4, 7:3, and 8:2) are higher than for the agarose SN hydrogel. For example, 6:4 DN hydrogels exhibit around 150% Young's Modulus, 260% toughness, and 375% fracture stress increase compared to agarose SN hydrogels (Figure 1B,C). The strain at break is similar for DN and agarose hydrogels, though. This can be justified by the presence of the charged copolymer, which forces agarose chains to stretch, consistent with the concept of a prestrained (agarose) network, resulting in a reduced capacity for strain during the mechanical test. The difference is, however, small considering the standard deviation of the strain at break (see overlapping error bars). Among the copolymer ratios of DN hydrogels, Young's Modulus, fracture toughness, strain at break, and tensile stress at break are similar for 30 and 40% AAc (7:3 and 6:4, respectively) but they increase notably as the mole percentage of AAc decreases to 20%. Hence, 3AgP(Am-co-AAc) 8:2 hydrogels have a higher load-bearing capacity. As described below, lower acrylic acid content contributes to the reduced electrostatic repulsion between copolymer chains, resulting in a smaller swelling ratio (water content). A narrower interchain distance may also lead to a higher extent of hydrogen bonding, entanglement,[25] and crosslinking density,[26] justifying that 8:2 DN hydrogels are stronger than 7:3 and 6:4 DN hydrogels.

Zeta potential, swelling ratio, and mechanical properties were measured at varying salt concentrations. The zeta potential was determined by an electrokinetic method (see the Experimental Methods section). This method is limited to electrolyte conductivities above 0.1 mS/m (KCl concentrations $\gtrsim$ 0.1 mM), and hence, the zeta potential in DI water cannot be measured. Despite the spectroscopy detection of COO^-, the zeta potential of the three DN hydrogels is negligible in 0.1 mM KCl solution. This suggests that counterions trapped inside the hydrogel minimize the charge density significantly. Counter-intuitively, as the concentration of KCl solution increases further, the zeta potential becomes increasingly negative, suggesting that the surface charge density increases with salt concentration (Figure 1D). The pH decreases from 6.1 to 5.65 when the concentration of KCl increases to 1 mM, and hence, it cannot justify the increasing negative zeta potential, as the decrease in pH should reduce the number of dissociated carboxylic groups.[27]

This conundrum can be addressed by taking the swelling ratio of the hydrogels into consideration. As-prepared hydrogels were equilibrated first in DI water (pH 6) for 24 h before measurement of the swelling ratio in KCl solution at concentrations between 0.1 and 100 mM; see the Experimental Methods section. Upon equilibration in DI water, DN hydrogels swell to different extents compared to the synthesis volume (Figure 1E). This is justified by the further dissociation of carboxylic groups at the pH of 6, which is larger than the synthesis pH (∼5). For reference, the swelling ratio of agarose SN hydrogels in water is 33, and hence, the DN notably reduces swelling compared to the reference agarose gel. By increasing the KCl concentration, the swelling ratio of the 6:4 and 7:3 DN hydrogels exhibits a nonmonotonic change, with a minimum at ∼0.1 mM, while the change of the swelling ratio of 8:2 DN hydrogels is insignificant in comparison. 6:4 and 7:3 DN hydrogels consistently display higher swelling ratios compared to 8:2 DN hydrogels at all salt concentrations.

The equilibrium swelling ratio of the DN hydrogels should be given by the balance between osmotic pressure, electrostatic repulsion, and elastic energy. The gradient of osmotic pressure between the hydrogel and its surrounding solution leads to the diffusion of water molecules into the charged hydrogels to lower the charge concentration difference inside the hydrogel compared to its surroundings. Swelling is also promoted by the electrostatic repulsion between polymer segments with unscreened charge. However, the swelling is restricted by the stretching of the first (stiffer) network. The largest AAc content in 6:4 DN hydrogels justifies the highest swelling ratios exhibited by these DN hydrogels in water.

The decreasing trend of the swelling ratio with increasing KCl concentration in the surrounding solution is attributed to charge screening by mobile counterions. Because both the zeta

https://doi.org/10.1021/acsami.3c00949
ACS Appl. Mater. Interfaces 2023, 15, 20495−20507

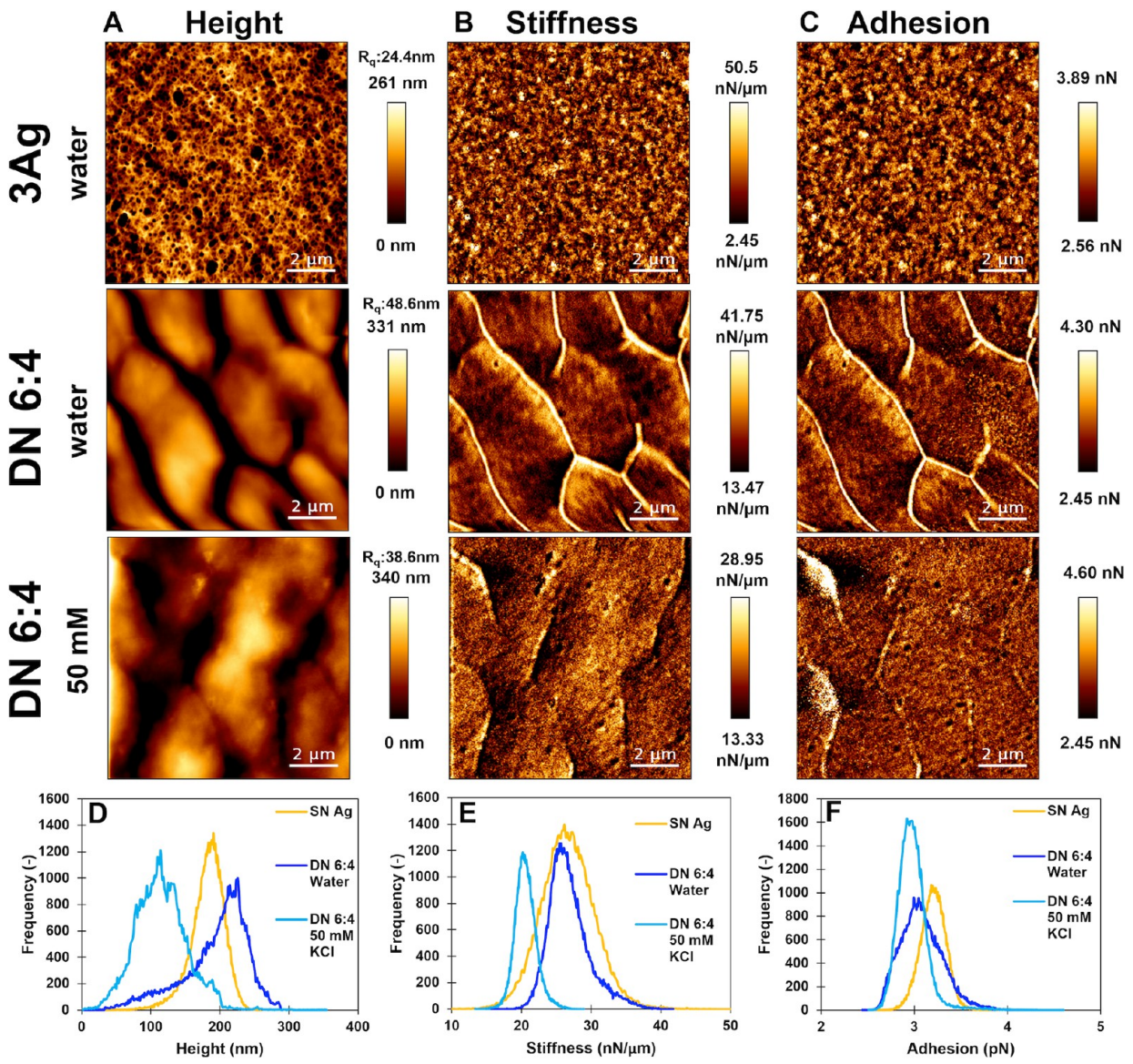

Figure 2. QI images of (A) height, (B) surface stiffness, and (C) adhesion of 3Ag SN hydrogel (top) and 3AgP(Am-co-AAc) 6:4 DN hydrogel (center) in water and in 50 mM KCl (bottom). (D–F) Corresponding histograms for the QI height, stiffness, and adhesion images in A–C.

potential and swelling ratio of agarose SN hydrogels do not significantly vary with salt concentration (-5.1 ± 0.8 mV, 31 ± 2 (−)), the intrinsic charge of the copolymer, which comes in the form of deprotonated acrylic acid groups (COO^-), is key in the responsive behavior of the DN hydrogels. Mobile counterions (K^+) in the surrounding solution can diffuse into the hydrogel microstructure to partially screen COO^- charges. With higher KCl concentration, there is a higher amount of mobile K^+ counterions that can screen COO^- groups in the hydrogels and decrease the effective charge, the electrostatic repulsion, and thereby, the swelling ratio. An increasing salt concentration can also promote a decrease in the swelling ratio to counterbalance the osmotic pressure gradient provided by the mobile counterions. As the bulk volume decreases, deprotonated acrylic acid groups in the chains become increasingly densified in the near-surface region. Hence, the charge-per-area increase justifies the higher zeta potential upon gel collapse. Comparing the three copolymer ratios, 6:4 displays the highest zeta potential, followed by 7:3 and finally 8:2. This is attributed to the higher acrylic acid content, and thereby, concentration of COO^- incorporated into the 6:4 DN hydrogels during synthesis.

Agarose SN hydrogels are weakly charged due to the presence of sulfate groups.[28] As mentioned earlier, increasing KCl concentration from 1 to 100 mM leads only to minor changes of the zeta potential and swelling ratio of the SN hydrogels, which indicates that counterions do not enter the network to screen the charge. For polymer brushes, this behavior has been labeled as "charged" polymer brushes,[29] which implies that the osmotic pressure gradient—as the counterions stay out of the polymer brush—becomes irrelevant compared to the uncompensated electrostatic repulsion between charged monomers, and the polymer brushes do not collapse with increasing salt concentration. Agarose SN hydrogels could behave in a similar fashion. The dominance of the electrostatic repulsion (as charges are not screened) would justify the small variation of the swelling ratio and zeta potential of agarose SN hydrogels with salt concentration. Therefore, despite being charged, agarose SN hydrogels are not responsive within the investigated range of KCl concentration.

https://doi.org/10.1021/acsami.3c00949
ACS Appl. Mater. Interfaces 2023, 15, 20495−20507

Tensile tests were performed on 6:4 DN hydrogels after equilibration for 24 h in 10 mM KCl solution; Figure 1F compares results on hydrogel samples from the same batch equilibrated either in water or in KCl solution. Mechanical properties are enhanced in 10 mM KCl compared to water. Hydrogels become stiffer in KCl as inferred from the 30% increase in Young's Modulus from around 600 to 800 kPa. Interestingly, hydrogels also become more ductile by allowing 40% increase in fracture strain from around 50 to 70%. Fracture toughness shows a 100% improvement, which is expected since fracture stress and strain of the hydrogel are higher in 10 mM KCl than in water.

Enhancement of the mechanical properties is attributed to the swelling behavior. As explained earlier, volume collapse happens when hydrogels are equilibrated in salt solution due to the screening of negative charge in the copolymer. This is expected to release (partially) strain energy of the agarose network, which now has a greater capacity for deformation before the network eventually fractures. Denser entanglements[25] between first and second networks could also result in more effective energy dissipation across both networks during fracture. Both the entropic consideration and the energy dissipation can contribute to the increased toughness. Furthermore, these results demonstrate that mechanical properties of charged DN hydrogels can be tuned by changing salt concentration.

Since 6:4 DN hydrogels exhibit greater sensitivity to salt concentration, it is hypothesized that they allow the highest tunability of surface properties, also under an applied electric potential. Thus, 6:4 DN hydrogels were selected as the representative composition for further studies.

2.2. Grain-like Topography, Adhesion, and Stiffness of 6:4 DN Hydrogels. Surface properties of 3AgP(Am-co-AAc) 6:4 DN hydrogels were characterized by atomic force microscopy (AFM) using quantitative imaging (QI) mode. QI performs a series of fast force curves at every pixel of the image. It provides simultaneous readings of surface height (topography), stiffness, and adhesion. A small load (~3 nN) and a fast approach velocity (200−250 μm/s) are applied to reduce deformation so that soft matter interfaces like hydrogels can be imaged. The hydrogel was imaged in a custom-made membrane cell that ensured the imaging in an aqueous environment and minimized evaporation of solution.

QI images of the 6:4 DN hydrogel in water revealed a heterogeneous surface structure composed of soft swollen grains and stiff grain boundaries, which significantly differs from the agarose single network (Figure 2). The adhesion to the grain boundary was also higher than to the grains, which is consistent with the higher water content of the grains. Note that copolymer SN hydrogels are so soft that imaging was not possible. Based on this, the hydrogel surface is consistent with the enrichment of agarose in the grain-boundaries surrounding copolymer-rich grain-like regions; see an illustration in Figure 3A. Each hydrogel sample was also imaged in KCl solution of increasing concentration (1, 10, 20, and 50 mM) after equilibration for 24 h in each solution (Figures 2 and S3). The same hydrogel was preserved for the entire range of solutions for fair comparison of surface properties. While every effort was made to image the same spot on the hydrogel, this was not possible due to the ex situ equilibration of the hydrogel. However, the images of multiple areas revealed a uniform response to salt concentration.

As the KCl concentration increases, the height of the grains decreases, which is consistent with the collapse of the charged copolymer and attributed to charge screening and decrease in the osmotic pressure gradient. Meanwhile, no swelling of the grain boundaries was observed, consistent with the enrichment of agarose surrounding the grain-like regions. Overall, stiffness and adhesion maps become more homogeneous with increasing KCl concentration, while the average values decrease; see histograms in Figure 2E,F. It is possible that the release of tension in the agarose network upon collapse of the copolymer-rich regions justifies the decrease of the surface stiffness. The decrease in adhesion may be associated with the increased repulsion between the hydrogel and the AFM tip as the charge density increases. Unfortunately, this hypothesis cannot be directly tested via surface force measurements because it is not possible to distinguish between electrostatic and steric (polymer-induced) repulsion, as well as deformation of the soft surface. However, Figure 1D shows that the zeta potential is more negative in 10 mM than in water, which supports that the

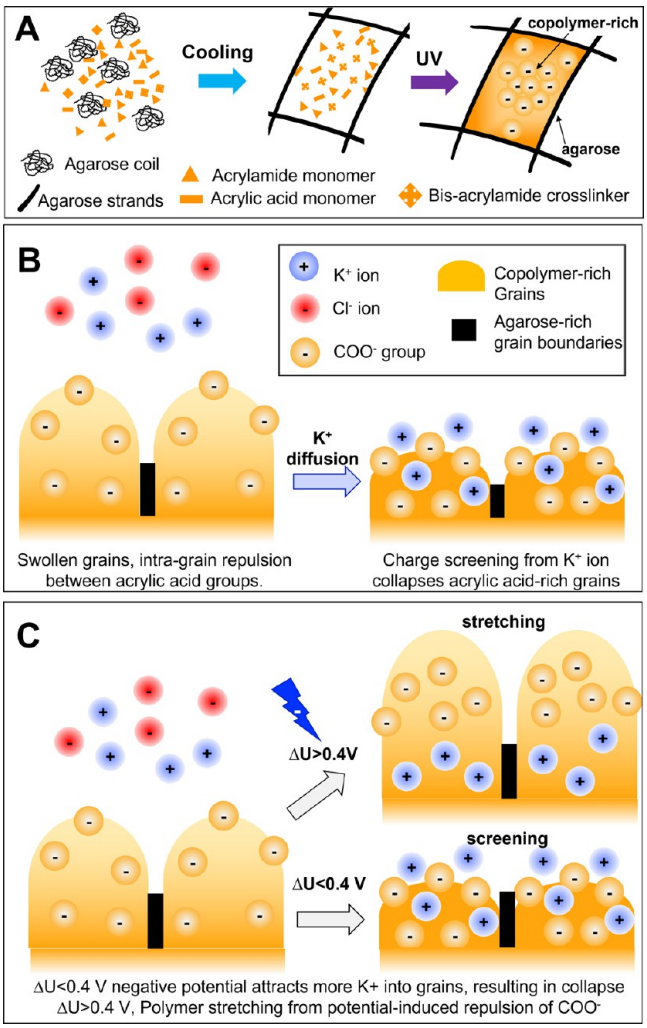

Figure 3. Illustration of the DN hydrogel surface structure and of the stimulus response. (A) Formation of the microstructure during synthesis. The top view shows grains and grain boundaries (agarose). A gradient in composition in the grains is inferred from experiments, with grain cores being copolymer-rich and grain edges composed of copolymer-poor regions. The transparency gradient corresponds to copolymer/charge density. (B) Response of the hydrogel near-surface region to the addition of salt (KCl) and (C) to an applied potential. As the swelling (collapse) of the copolymer happens due to changes in salt concentration or pH, the height difference of the grains increases (decreases). This also influences adhesion and friction; see text.

https://doi.org/10.1021/acsami.3c00949
ACS Appl. Mater. Interfaces 2023, 15, 20495−20507

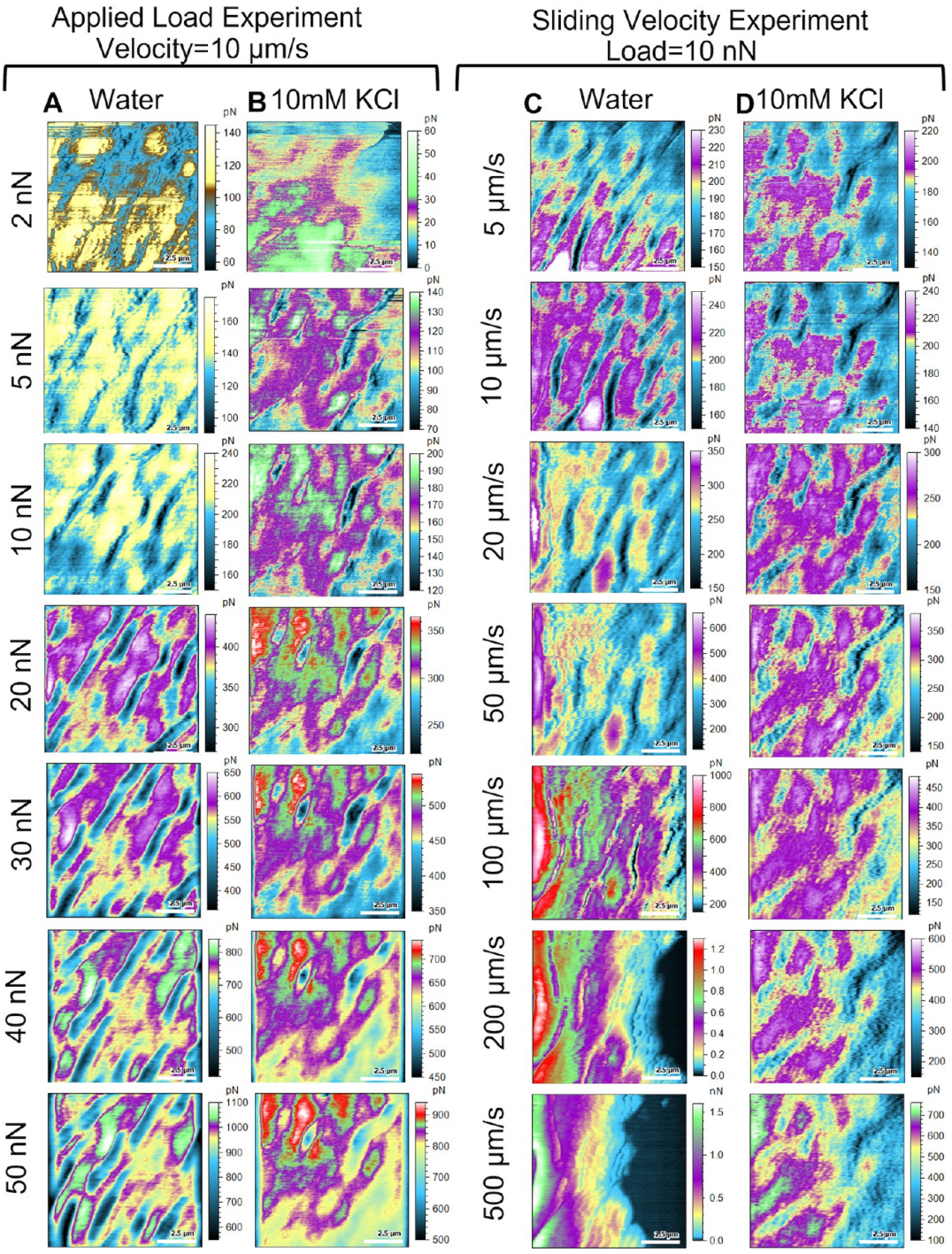

Figure 4. Friction maps as a function of applied load (A) in water, and (B) in KCl 10 mM, and as a function of sliding velocity (C) in water, and (D) in KCl 10 mM. Original images can be found in the SI (Figures S5 and S6). Different z-scales are used in each plot. Loads 2−50 nN correspond to Hertzian stresses 8−24 kPa. An example of a friction loop extracted from a friction image is shown in Figure S7.

tip, negatively charged due to the present surface oxide layer−,[30] will experience a stronger repulsive interaction while approaching the hydrogel surface. Figure 3B displays schematics of the proposed response of the interface to increased salt concentration.

2.3. Heterogeneous Frictional Characteristics of DN Hydrogels and Responsiveness to Salt Concentration. Friction images were generated using contact mode imaging by lateral force microscopy (LFM) to visualize the frictional characteristics of the DN hydrogels. A blunt silicon tip (R = 2.8 μm) was used to avoid puncturing the relatively soft hydrogel surface during contact mode imaging; see Figure S4. In contact mode imaging, the tip applies a load and slides at constant velocity along each new line from the left to the right (trace), and it returns to the origin from the right to the left (retrace); then it lifts and moves up to the next scan line and applies the same load, and the scanning process is repeated. Trace and retrace height and lateral deflection images are taken simultaneously, while friction images are generated from the lateral deflection images.[31] Friction studies were conducted in equilibrium with

https://doi.org/10.1021/acsami.3c00949
ACS Appl. Mater. Interfaces 2023, 15, 20495−20507

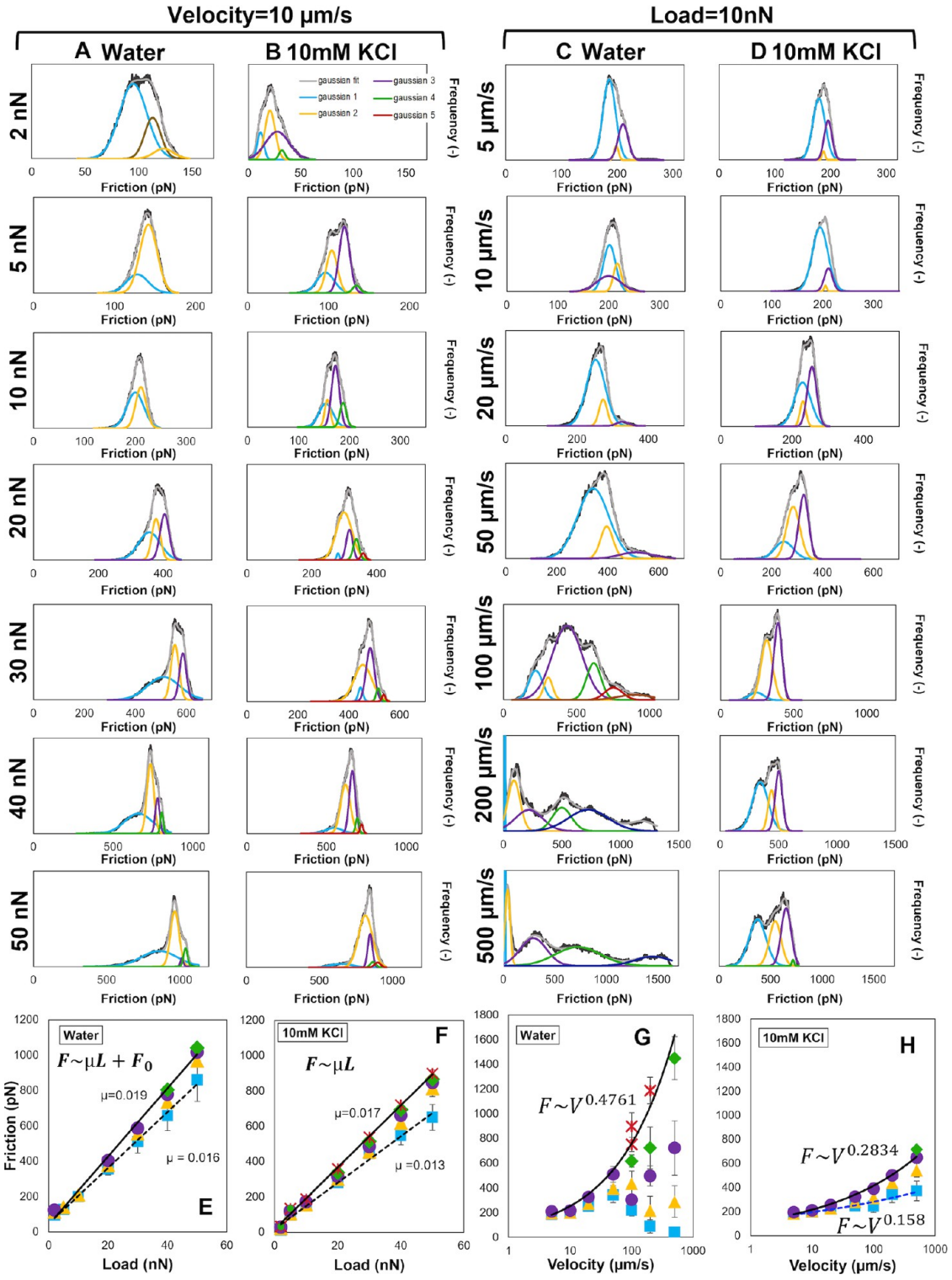

Figure 5. Histograms of friction response to load (columns A, B) and velocity (columns C, D). Pixel values of all friction images (Figure 4) were exported to histograms (in black). The histograms were fit (in gray) by the sum of five Gaussian distributions (colored lines in blue, yellow, purple, green, and red). The color code is the same as in the friction images. The gaussian distribution in brown (A, 2nN) results from the partial contact between tip and hydrogel surface at 2nN in water. Friction vs (E, F) load and (G, H) velocity; the data points correspond to the means of each Gaussian distribution in water (E and G) and 10 mM KCl (F and H). The colors correspond to the gaussian distributions (1−5) shown in A−D.

either DI water or 10 mM KCl solution. Details are reported in the Experimental Methods section.

To measure friction as a function of applied load, the sliding velocity was maintained constant at 10 μm/s. Figure 4A shows the friction images in water while the corresponding height and lateral deflection images are shown in Figure S5. Because the tip is blunt, the resolution of the topographic images in contact mode is not as good as in QI imaging, but it is sufficient to resolve the grain-like microstructure. At the smallest load of 2 nN, friction maps display two different regions of high and low

https://doi.org/10.1021/acsami.3c00949
ACS Appl. Mater. Interfaces 2023, 15, 20495−20507

friction (gold and blue, respectively). By increasing the load to 5 nN, height images do not change, but there is an increase in height difference and friction, as inferred from the expansion of the yellow region. The height difference increase might be because the tip occasionally loses contact with the hydrogel surface at 2 nN; in this case, a water film could provide efficient lubrication; as often invoked by Klein's hydration lubrication.[32,33] Partial loss of contact at 2 nN happens in both DI water and KCl solution. Increasing load above 5 nN flattens the grains, as inferred from the height images, but this is more prominent in water than in KCl solution, likely due to the collapse of the charged copolymer in salt solution, which reduces the heterogeneity of the surface and of the frictional response.

Pixel values of all friction images were exported to histograms (Figure 5, black lines). In water (Figure 5A), friction histograms for loads of 2, 5, and 10 nN show singular peak values at ∼100, 150, and 200 pN, respectively. When load increases above 10 nN, friction histograms start to display a left shoulder. According to the colored friction maps, this left shoulder corresponds to the lower friction at grain boundaries. Peak friction values continued to increase to 390, 550, 750, and 960 pN with an increase of load to 20, 30, 40, and 50 nN, respectively. The presence of the left shoulders on the histogram at intermediate to high loads reflects the frictional response of a heterogeneous surface with two domains (grains and grain boundaries). Since the grain boundaries have a lower height than the grains, the AFM tip may have poorer tracking across the boundaries under low applied loads. Intermediate loads allow the AFM tip to contact the hydrogel surface more firmly and to squeeze into the boundaries, which explains the appearance of the shoulder.

To account for the heterogeneities in friction images, we determined the friction contribution of each region (or phase) by deconvoluting the histogram into multiple Gaussian distributions; each Gaussian distribution has the same color as the corresponding region in the friction image; see the legend in Figure 5B (2 nN). Grain boundaries consistently reflect the lowest friction (deep blue), while grains constitute the second friction region (gold). At intermediate to higher loads, grain friction further bifurcates into two sub-contributions (gold and purple). This bimodal contribution to the friction histogram indicates the existence of composition fluctuations within the grains, and hence, it suggests that the grains are not monophasic, presumably revealing the presence of copolymer-rich and copolymer-poor regions. This could be due to a gradient in the volume fractions of copolymer and water or to the coexistence of agarose and copolymer with spatially varying volume fractions within the grains. In either case, the nonuniform copolymer distribution leads to a spatially varying friction force when loads are sufficiently high to probe these regions. A green region (high friction) emerges at high loads, which corresponds to the highest asperities on the hydrogel surface (see height images in Figure S6). Although this may suggest the existence of a third phase in the grains, this happens when the tip flattens the tallest asperities at high loads, creating a temporary spike in local friction around the asperities. Hence, the green region is thought to result from the effect of the surface roughness on friction.

The mean values and the standard deviation of each Gaussian distribution are shown in Figure 5E. A linear relation is obtained between the average friction of each Gaussian distribution and load in water, with finite friction force at zero load ($F_0 \sim 120$ pN). This is in line with Derjaguin's modified version of Amonton's law for adhering surfaces.[34] The coefficient of friction ranges between 0.016 and 0.019 based on the lowest and highest linear fits, respectively.

In 10 mM KCl, the grain boundaries become more distinct at higher loads, and friction at these boundaries is smaller than in the grains (Figure 4B). Friction histograms also display a shift of the friction peak to higher values with load, though overall friction is smaller than in water (Figure 5B). Note the smaller friction values for the same color code in KCl compared to water (Figure 4A). The left shoulder in friction histograms—corresponding to grain boundaries—appears only above 40 nN, i.e., at higher values than in water. The average friction value (peaks) of each gaussian distribution also increases linearly as a function of the normal load, with friction coefficients ranging between 0.013 and 0.017, thus a bit lower than in water (Figure 5F). In KCl, Amonton's law (for nonadhering surfaces) describes well the relation between friction and load ($F_0 \sim 0$), in contrast to the results in water. The observed differences can be explained by the more significant electrostatic repulsion between tip and hydrogel surface in 10 mM KCl compared to water. In addition to this, the less swollen state of the hydrogel justifies the smaller roughness in the salt solution (Figure S3), which is also expected to contribute to reducing friction.

It is worth mentioning that the insight provided by friction loops, the traditional method to measure friction by AFM (Figure S7), is included in friction images. However, friction images are more appropriate to describe (2D) surface heterogeneities.

2.4. Lubrication Mechanisms. In velocity-dependent friction measurements at constant load of 10 nN in DI water, the tip tracks the surface well below 200 μm/s and reveals similar friction heterogeneities as load-dependent friction measurements (Figure 4C). The lowest friction (deep blue) appears in grain boundaries. Meanwhile, friction at grains shows two to three regions with the increase in velocity (gold, purple, and green). Generally, grain cores exhibit higher friction, followed by grain edges, and finally grain boundaries. Importantly, the difference between height trace and retrace images is enhanced with velocity (Figures S8 and S9), which indicates that the gel deforms viscoelastically, i.e., the gel deforms under the applied load during trace and does not recover before retrace. The viscoelastic behavior of the hydrogel surface was confirmed in indentation measurements, which are summarized in Figure S10. Such viscoelastic deformation contributes to the frictional dissipation and more so with an increase in velocity.

Furthermore, as the velocity increases to 200 μm/s, friction becomes much higher on the left than on the right side of the friction image; see the black regions on the right side of images. Concurrently, the corresponding height trace and retrace images do not display well the surface topography (Figure S8), and single friction loops in this region reveal the partial overlap of the trace and retrace (Figure S11). This implies the tip lifts toward the right side of the friction maps, resulting in a prominent decrease of the friction force since a water film provides more efficient lubrication. There also appears to be high static friction (red) on the left side of the friction maps. Note that the dark left edge in the trace height image together with the cluster in the center of the image indicates that the tip initially sticks to the hydrogel surface and pushes the material to the right, before sliding starts in the trace direction. Hence, it is possible that the red region reflects pilling-up effects.[35] These results indicate that there is a sliding asymmetry at high sliding velocities.

The influence of the sliding velocity on friction in DI water is complex (Figure 5C,G). Friction initially increases with sliding

https://doi.org/10.1021/acsami.3c00949
ACS Appl. Mater. Interfaces 2023, 15, 20495−20507

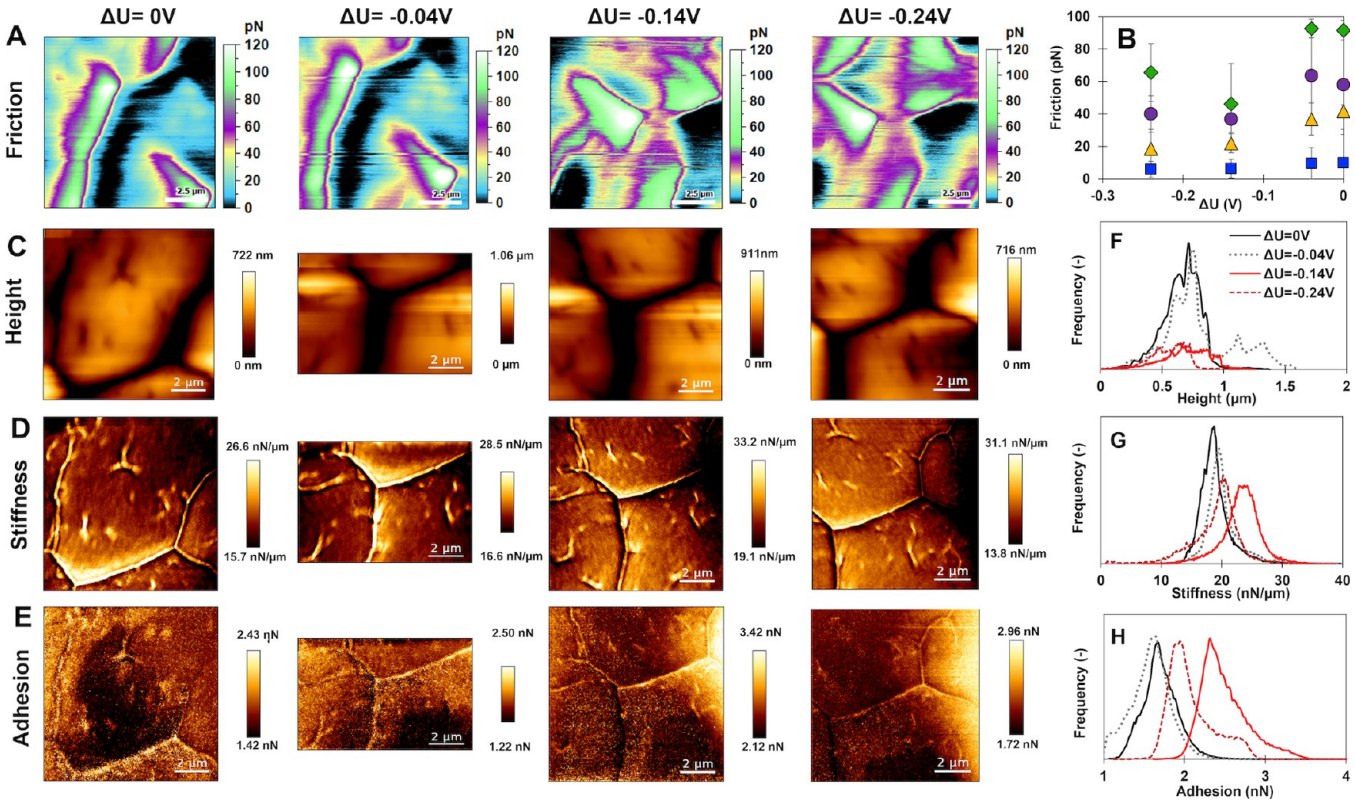

Figure 6. Electrotunability of 6:4 DN hydrogel friction in 10 mM KCl. (A) Friction images with applied potential, (B) average friction force in each region extracted from gaussian fits to friction histograms, (C–E) QI images of hydrogels subjected to various electric potentials, (C) height, (D) stiffness, and (E) adhesion. Histograms corresponding to (F) height, (G) stiffness, and (H) adhesion images in (C–E).

velocity and starts to diverge around 50 μm/s. Above 50 μm/s, there is a decrease in the friction contribution from some regions (blue, yellow, purple), which is attributed to the observed hydrodynamic lift; meanwhile, the tallest asperities (green, red) remain in contact. Hence, a water film starts developing and partially separates the hydrogel and the tip along the sliding distance. It is reasonable to expect that higher velocities—not achievable with our AFM—could yield full fluid film lubrication. By fitting a power law, friction is observed to scale with sliding velocity with an exponent of 0.48. This is slightly lower than the exponent of 0.5 found by Shoaib et al. for polyacrylamide SN hydrogels[35] and Pitenis et al. for the Gemini interface of polyNIPAM SN hydrogels.[36]

The velocity-dependence of the friction images was shown to be tunable upon equilibration in 10 mM KCl (Figure 4D). Like in water, the lowest friction was observed in grain boundaries (deep blue region). The distinct friction of grains and boundaries is maintained at slow sliding velocities, but the contrast is less significant than in water. This is likely due to the collapse of the surface structure, as inferred for the smaller height difference in KCl compared to water (Figure S3). The much narrower friction histograms also reflect the more homogeneous frictional characteristics of the gel in KCl compared to DI water (cf. Figure 5C,D). Closer inspection of height trace and retrace images also reveals the partial lift of the tip at higher velocities, but to a much smaller extent than in water (Figures S8 and S9). Furthermore, the highest friction (red in water, left edge) was not observed in KCl. In water, the red regions were attributed to pilling-up and/or static friction. Figures 2 and S3 show the greater topological unevenness and more deformability (smaller stiffness) of the gels in water, and hence, pilling-up effects appear to be more significant than in 10 mM KCl solution. In addition, since the zeta potential is more negative in KCl solution, the repulsion between the tip and hydrogel is expected to be higher than in water, and therefore, the adhesive contribution to friction and stiction should decrease.

Overall, friction in 10 mM KCl increases steadily with sliding velocity. This response correlates with reduced pilling-up and hydrodynamic lift effects. Fitting a power law to the velocity-dependent friction leads to an exponent between 0.16 and 0.28 (Figure 5H, and hence, smaller than in water (0.48). The scaling exponents found here are similar to those of other DN hydrogels.[2] Shoaib et al. prepared DN hydrogels composed of agarose and polyacrylamide (AgPAAm) in water-DMSO mixtures.[23] Using an analogous setup to ours, they found power law exponents ranging from 0.52 to 0.61. The partially collapsed gel in 50% DMSO exhibited a lower exponent compared to water, as we also found for KCl compared to water, but our exponents are smaller. Note that AgPAAm DN hydrogels are uncharged, and the viscosity of DMSO is much greater compared to 10 mM KCl, both of which can justify the enhanced frictional dissipation, and thereby the higher exponents found for AgPAAm DN hydrogels in that previous work.

Previous studies from our group have shown velocity-weakening and velocity-strengthening regimes, also for AgPAAm DN hydrogels.[21,35,37] Adhesive effects dominated the frictional dissipation below a transition velocity, while viscous shear of the near-surface region of the gel dictated friction above it. The lack of a velocity-weakening frictional response for 6:4 DN hydrogels suggests that the velocities used in this work are too high to evaluate the adhesive scaling regime

https://doi.org/10.1021/acsami.3c00949
ACS Appl. Mater. Interfaces 2023, 15, 20495−20507

and/or the adhesion to the sliding tip is too small, even in water. The results described above indicate that the viscous shear of the near-surface polymer network, its viscoelastic deformation, and the lubrication by a water film (at small loads or sufficiently high sliding velocities) contribute to the frictional dissipation at the sliding interface of these DN hydrogels.

2.5. Responsiveness of 6:4 DN Hydrogel Friction to Electric Potential. The frictional response to an electric potential is summarized in Figure 6. Applied potential was recorded with respect to the open circuit potential (OCP), i.e., $\Delta U = V_{applied} - V_{OCP}$, with $V_{OCP} = -0.76$ V. Based on the height upon trace and retrace, it is concluded that the tip tracks the surface well in both directions (Figure S12). However, there are differences between the trace and retrace heights of those structures, likely due to viscoelastic effects. That is, the surface of the hydrogel deforms during trace but does not fully recover before retrace. Nonetheless, load and sliding velocity were kept constant in these experiments, so that any effects of viscoelastic response remained approximately constant throughout the measurements.

Friction images (Figure 6A) remain relatively unchanged near the OCP, but they change when ΔU decreases to −0.14 and −0.24 V. To quantify these changes, friction histograms were extracted from each friction image (Figure S12). The histogram at each potential is wide and exhibits various peaks, which reflects the heterogeneities of the surface. Each histogram was fit by four superposed gaussian distributions, revealing four regions in the friction images: a water film in areas too deep to track (deep blue to black); agarose rich boundaries (bright blue); copolymer-poor grain edges (gold to purple); and copolymer-rich grain cores (green). Figure 6B shows that friction decreases with potential below $\Delta U = -0.04$ V, reaching a minimum at $\Delta U \sim -0.14$ V. As potential becomes more negative, friction increases again, suggesting a turning point at around −0.14 V. The change is more significant for green (copolymer-rich), purple, and gold (copolymer-poor) regions, while the change in friction of the blue region is insignificant. The greatest change (~50 pN) in friction occurs in the green region (grain core), where deprotonated acrylic acid groups are hypothesized to be the most concentrated; see the cartoon in Figure 3C. This is because charged acrylic acid groups are expected to respond the most significantly to the electric potential and/or counterion-induced charge screening effects.

To understand the frictional response to the electric potential, the corresponding change of topography, stiffness, and adhesion was determined by QI imaging (Figure 6C−H). At $\Delta U = -0.04$ V, the hydrogel initially swells toward a maximum (height difference ~ 1.06 μm). As the potential further decreases, the hydrogel collapses, and the height decreases toward 716 nm at $\Delta U = -0.24$ V. Concurrently, stiffness increases with potential, and a maximum is observed at $\Delta U = -0.14$ V. Thereafter, stiffness (see low limit) decreases significantly from 19.1 to 13.8 nN/μm; see also the histogram in Figure 6G. Here, it is possible that the agarose-rich phase may have reached a maximum strain at ~ −0.14 V, hindering the copolymer-rich phase to swell further when the potential further decreases. Adhesion remains relatively constant near OCP, and then it increases sharply from 2.50 to 3.42 nN at $\Delta U = -0.14$ V. After peaking at −0.14 V, it decreases as the potential is further decreased to −0.24 V; see also the histogram in Figure 6H. The minimum friction corresponds to the condition of highest stiffness and adhesion in QI images, and hence, the highest adhesion does not correlate with the highest friction. It is thus concluded that the contribution of adhesive interactions to friction is small, likely because of the small contact area of these stiffer regions. Overall, less energy is dissipated at −0.14 V, resulting in lower friction.

Note that, while the comparison above highlights that the increase (decrease) of average stiffness happens concurrently with the increase (decrease) of average adhesion, there are heterogeneities within the grains in each image that show the opposite. Indeed, there are low-stiffness regions (dark, see arrow) that correspond to high (bright) adhesion regions, likely due to the larger contact area of these softer regions. This varying behavior could result from the gradients in copolymer concentration within the grains, as described earlier.

The nonmonotonic changes in QI images and friction suggest the action of competing mechanisms under an applied potential; see the cartoon in Figure 3C. On the one hand, volume expansion originates from a combination of electrostatic repulsion and osmotic pressure-induced swelling. That is, when a negative potential is applied, it drives the diffusion of K^+ counterions into the hydrogel. The increase in ionic concentration causes osmotic pressure to increase,[38] and the gel to swell. This is combined with the repulsive force acting on the charged polymer, which results in the overall swelling of the gels as inferred from the height difference increase. The stiffness increase could be due to the blunt tip pressing against a more stretched polymer network. The adhesion increase can be justified by the weaker net repulsion between the tip and hydrogel because of electrostatic screening by diffused counterions. On the other hand, a volume collapse can result from charge screening by counterions and the enhanced entropy elasticity of a less charged polymer network, which can adopt more random conformations.[38] At potentials below −0.14 V, the osmotic pressure and the electrostatic repulsion of the charged polymer dictate the change of surface properties and cause friction to decrease as the hydrogel swells with increasing potential. Electrostatic screening and/or entropy elasticity take over above −0.14 V, causing the gel to collapse and friction to rise.

3. IMPLICATIONS

Although the friction coefficients of the investigated DN hydrogels (~0.01 to 0.02) did not rival the superlubricity achieved by other hydrogels,[15,39] they are comparable to articular cartilage ($\mu \sim 0.001$ to 0.04).[3] Similar friction coefficients to natural tissue may inspire new designs of more biocompatible replacements. If polymer is charged, the strength of such replacements and thus their durability could be enhanced by the synovial fluid containing salt ions.[1] There are other avenues to improve the mechanical performance of the hydrogels, such as the addition of stronger bonds,[40,41] however at the cost of reducing the tunability of hydrogel properties. On the other hand, agarose is physically crosslinked through hydrogen bonding and such noncovalent interactions could be suitable for achieving self-healing behavior.[42] However, the chemical crosslinking in the copolymer precludes self-healing, and hence, targeting self-healing would require a modification of the second network in these gels.

Not only the durability but also the stimuli-selectivity have been highlighted as areas for improvement in hydrogel soft robots.[13] Our study shows the capability to dynamically control friction and adhesion via an electric potential. Furthermore, the heterogeneous surface structure of the hydrogel, resembling grain and grain boundaries, enables the spatial control of surface properties like surface stiffness, friction, and adhesion. These

https://doi.org/10.1021/acsami.3c00949
ACS Appl. Mater. Interfaces 2023, 15, 20495−20507

advancements build upon the bulk property changes that were previously demonstrated for soft robots made of DN[43−45] and SN[6] hydrogels. Although we have not explored the conductivity of our DN gels yet, salt-based hydrogel modifications could potentially be applied to achieve high conductivity, while improving strength.[46] Improving the mechanical behavior of these DN hydrogels while maintaining its stimulus-responsive behavior may be possible by varying the mole ratio of the copolymer to agarose. For example, the decrease of the copolymer content leads to a reduction of the swelling ratio of the charged copolymer within the agarose network and converts the grain-like morphology into a micellar surface topography. Lamellar microphase separations and colloidal microstructures have been also achieved with this copolymer and its modifications.[47,48] This opens new opportunities to modify the interfacial behavior of hydrogels, which is the scope of our current studies.

4. CONCLUSIONS

We have examined the tunable properties of charged DN hydrogels composed of a first network (agarose) and a second network (charged copolymer, AAm-co-AAc) and their relationship to microstructure. We demonstrate mechanical strengthening by salt concentration, which is attributed to the network densification resulting from the partial hydrogel collapse induced by charge screening and enhanced entropy elasticity. We have also scrutinized the interfacial behavior via topography, adhesion, and friction images. Friction images and their deconvolution in Gaussian distributions provide direct visualization of the contribution of the individual networks in the DN hydrogel to friction. Friction mainly arises from the viscous shear of the polymeric networks, whereas hydrodynamic lift and viscoelastic deformation become more significant at higher sliding velocities. We can distinguish the friction characteristics of grain boundaries (agarose network) and grains (copolymer-rich and -poor) and identify the copolymer-rich phase as the main source of the stimulus responsive behavior. 10 mM KCl collapses the gel and increases charge density, which reduces friction despite the decrease in water content. An electric potential can swell (collapse) the gel, which increases (decreases) the water content and reduces (increases) friction.

The novelty of this work lies in the microstructure-level resolution of interfacial properties and friction of a charged DN hydrogel and the study of their stimuli-responsive behavior. Our findings provide greater insight into the microstructure-property relationship of DN hydrogels and the design strategies for tuning the mechanical strength and lubricity of these versatile soft materials, thereby promoting the development of DN hydrogel-based tissue replacements and soft robotics.

5. MATERIALS AND METHODS

5.1. Materials. Agarose (A4718), acrylamide 40% solution (A4058), *N*,*N*′-methylene bisacrylamide 2% solution (M1533), and acrylic acid 99% (147230), sodium hydroxide pellets (S5881), and a-ketoglutaric acid (75890) were used as received from Sigma-Aldrich. 5 M sodium hydroxide stock solution was prepared by dissolving pellets in deionized water. Initiator stock solution was prepared by dissolving 0.164 g of a-ketoglutaric acid powder in 1 mL of deionized water in an amber glass vial. Amber glass vials were utilized to shield the solution from premature exposure to UV light.

Hydrophobic substrate preparation: Dichlorodimethylsilane (440272) and toluene (179418) were used as received from Sigma-Aldrich. 25 mm rounded glass cover slips and microscope glass slides were purchased from VWR. 5 mM solution of dichlorodimethylsilane in toluene was prepared in a glass Petri dish. Next, glass cover slips and microscope glass slides were immersed in the solution overnight to produce hydrophobic coated glass substrates. Finally, the silanized glass were rinsed with DI water and dried with nitrogen blowing before use.

5.2. Hydrogel Preparation. Acrylamide (Am), *N*,*N*′-methylene-bisacrylamide (bis-Am), acrylic acid (AAc), and 5 M sodium hydroxide (NaOH) solution were added into a vacuum flask and degassed for 15 min. NaOH was added to adjust the solution pH to 5 to equalize the reactivity ratio between acrylamide and acrylic acid.[24] Meanwhile, 0.3 g of agarose powder was dissolved into a beaker of deionized (DI) water under stirring at 80 °C. The contents of the vacuum flask were then mixed into the beaker followed by the addition of a-ketoglutaric acid initiator solution. After briefly mixing for 15 s, a plastic dropper was used to deposit five drops of final mixture in between the hydrophobic silanized cover slip and microscope glass slide. This wet mixture was then cooled in a 4 °C cold room to allow agarose to gelate. Next, the glass and gel were exposed to UV light (Spectroline) for 1 h to polymerize and gelate the copolymer within the existing agarose network. The as-prepared hydrogels were then equilibrated in DI water (pH ∼ 6) for 24 h before testing. Specific quantities of chemicals used for each hydrogel can be found in Table 1. Practical limitations prevented us from the gelation of copolymer as the first network and agarose as the second network. Preparation of the agarose network required heating the precursor solution at 80 °C for several minutes to ensure helix-coil transition, but acrylamide has been shown to decompose around 84 °C. Furthermore, long heating time is required to allow agarose solution to diffuse into the pores of the copolymer hydrogel that would have further degraded the copolymer. As a result, we adopted agarose as the first network, mixing in the monomers required for the second network merely seconds before the final mixture was removed from the hot plate and deposited between the glass substrates.

5.3. Swelling Experiments. Swelling ratios of the hydrogels were calculated by comparing its fully hydrated weight against its dry weight. Fully hydrated weight refers to the weight of hydrogels that have been equilibrated in water (or KCl solution) for at least 24 h. Dry weight refers to the weight of hydrogels that were dried on a hot plate at 60 °C for at least 24 h. The swelling ratios reported were calculated by dividing the hydrated weight by the dry weight.

5.4. FTIR. An ATR-FTIR (Frontier FT-IR, Perkin Elmer) with a diamond head (400−4000 cm^{-1}) was used to characterize the functional groups present on the hydrogels. The reported data were reduced to the wavenumber range of 900−1900 cm^{-1} where the relevant functional groups were identified. The penetration depth of the analysis is approximately ∼2 μm, probing into the near surface microstructure.

5.5. Zeta Potential Measurement. Zeta potentials of the hydrogel surface were measured using SurPASS 3 (Anton Paar). Two rectangular strips of hydrogel were punched out (standard setup provided by Anton Paar) and mounted in the machine with a 100 μm gap between them. Solutions at the selected concentrations of KCl solution were then passed through the measuring cell. SurPASS outputs the zeta potential and goodness of fits. Data with goodness >95% were averaged and reported.

5.6. Tensile Test. The tensile test of hydrogels was performed using Dynamic Mechanic Analysis DMA Q-800 (TA Instruments) under controlled force mode and tension film clamp. A minimum of four and maximum of seven hydrogels were tested for each composition. The results are averaged, and the error bars give the standard deviation. Hydrogels were cut into rectangular strips measuring 25 mm long by 5 mm wide. These strips were then clamped in the instrument and tension force was applied at ramp rate of 3 N/min until fracture.

5.7. Surface Height, Stiffness, Adhesion, and Friction Measurements. An atomic force microscope (NanoWizard AFM, JPK Instruments) was used for surface measurements of hydrogels. AFM measurements were performed in a liquid environment with an in-house membrane cell setup. QI mode (Mikromasch HQ:CSC37/No Al) was used to obtain height, stiffness, and adhesion images with sharp silicon tips. Sader's method[49] was used to determine the normal spring constant, while a noncontact thermal noise method[50] was used for

https://doi.org/10.1021/acsami.3c00949
ACS Appl. Mater. Interfaces 2023, 15, 20495−20507

lateral calibration. The setpoint was 3 nN unless otherwise specified. For contact-mode AFM, sharp silicon tips were thermally blunted in a tube furnace at 1050 °C for 2 h. The blunt tip radius was estimated to be approximately 2.8 μm by reverse imaging on a silicon grating (Ted Pella Test Grating TGTZ-400) and fitting radius of curvature in Mountains SPIP software (DigitalSurf). The 3D tip model and fit are shown in Figure S4. Setpoint and scan velocity were varied as reported in the Results section. Friction images were postprocessed from contact mode lateral force images using JPK Data Processing (JPK Instruments) and Mountains software.

5.8. Electric Potential Experiments. A three-electrode cell was constructed with copper tape and aluminum foil as the working electrode, gold wire as the counter electrode, and silver wire as the reference electrode. Potentials reported are pseudo-Ag potentials and presented as the difference from its open-circuit potential (OCP). The cells were filled with 10 mM KCl solution as the electrolyte.

■ ASSOCIATED CONTENT

Supporting Information

The Supporting Information is available free of charge at https://pubs.acs.org/doi/10.1021/acsami.3c00949.

Representative stress strain curves and optical image of tensile test, original colored AFM QI and LFM images, blunt tip radius fitting in Mountains, indentation measurements, and friction loops (PDF)

■ AUTHOR INFORMATION

Corresponding Author

Rosa M. Espinosa-Marzal − *Department of Materials Science and Engineering and Department of Civil and Environmental Engineering, University of Illinois at Urbana-Champaign, Urbana, Illinois 61801, United States;* orcid.org/0000-0003-3442-2511; Email: rosae@illinois.edu

Author

Ming Jun Lee − *Department of Materials Science and Engineering, University of Illinois at Urbana-Champaign, Urbana, Illinois 61801, United States*

Complete contact information is available at: https://pubs.acs.org/10.1021/acsami.3c00949

Author Contributions

The manuscript was written through contributions of all authors. All authors have given approval to the final version of the manuscript.

Funding

National Science Foundation under grants CMMI 17-61696, CMMI 21-21681 and CMMI 21-54530.

Notes

The authors declare no competing financial interest.

■ ACKNOWLEDGMENTS

This article is based on work supported by the National Science Foundation under grants CMMI 17-61696, CMMI 21-21681 and CMMI 21-54530. Research was carried out in part in the Materials Research Laboratory Central Research Facilities, University of Illinois.

■ REFERENCES

(1) Milner, P. E.; Parkes, M.; Puetzer, J. L.; Chapman, R.; Stevens, M. M.; Cann, P.; Jeffers, J. R. T. A low Friction, Biphasic and Boundary Lubricating Hydrogel for Cartilage Replacement. *Acta Biomater.* **2018**, *65*, 102−111.

(2) Bonyadi, S. Z.; Demott, C. J.; Grunlan, M. A.; Dunn, A. C. Cartilage-like Tribological Performance of Charged Double Network Hydrogels. *J. Mech. Behav. Biomed. Mater.* **2021**, *114*, No. 104202.

(3) Chen, Q.; Zhang, X.; Chen, K.; Feng, C.; Wang, D.; Qi, J.; Li, X.; Zhao, X.; Chai, Z.; Zhang, D. Bilayer Hydrogels with Low Friction and High Load-Bearing Capacity by Mimicking the Oriented Hierarchical Structure of Cartilage. *ACS Appl. Mater. Interfaces* **2022**, *14*, 52347−52358.

(4) Gu, Z.; Huang, K.; Luo, Y.; Zhang, L.; Kuang, T.; Chen, Z.; Liao, G. Double network Hydrogel for Tissue Engineering. *WIREs Nanomed. Nanobiotechnol.* **2018**, *10*, No. e1520.

(5) Pan, Y.-S.; Xiong, D.-S.; Ma, R.-Y. A Study on the Friction Properties of Poly(vinyl alcohol) Hydrogel as Articular Cartilage against Titanium Alloy. *Wear* **2007**, *262*, 1021−1025.

(6) Morales, D.; Palleau, E.; Dickey, M. D.; Velev, O. D. Electro-Actuated Hydrogel Walkers with Dual Responsive Legs. *Soft Matter* **2014**, *10*, 1337−1348.

(7) Kang, Y.-W.; Woo, J.; Lee, H.-R.; Sun, J.-Y. A Mechanically Enhanced Electroactive Hydrogel for 3D Printing using a Multileg Long Chain Crosslinker. *Smart Mater. Struct.* **2019**, *28*, No. 095016.

(8) Chen, Q.; Chen, H.; Zhu, L.; Zheng, J. Fundamentals of Double Network Hydrogels. *J. Mater. Chem. B* **2015**, *3*, 3654−3676.

(9) Zhang, B.; Gao, Z.; Gao, G.; Zhao, W.; Li, J.; Ren, X. Highly Mechanical and Fatigue-Resistant Double Network Hydrogels by Dual Physically Hydrophobic Association and Ionic Crosslinking. *Macromol. Mater. Eng.* **2018**, *303*, No. 1800072.

(10) Yang, Q.; Gao, C.; Zhang, X.; Zhao, X.; Fu, Y.; Tsou, C.; Zeng, C.; Yuan, L.; Pu, Z.; Xia, Y.; Sheng, Y.; Fang, Y. Dual-Responsive Shape Memory Hydrogels with Self-Healing and Dual-Responsive Swelling Behaviors. *J. Appl. Polym. Sci.* **2021**, *138*, 50308.

(11) Gong, J. P. Why are Double Network Hydrogels so Tough? *Soft Matter* **2010**, *6*, 2583.

(12) Gong, J. P.; Katsuyama, Y.; Kurokawa, T.; Osada, Y. Double-Network Hydrogels with Extremely High Mechanical Strength. *Adv. Mater.* **2003**, *15*, 1155−1158.

(13) Lee, Y.; Song, W. J.; Sun, J. Y. Hydrogel Soft Robotics. *Mater. Today Phys.* **2020**, *15*, 100528.

(14) Peng, K.; Yang, K.; Fan, Y.; Yasin, A.; Hao, X.; Yang, H. Thermal/Light Dual-Activated Shape Memory Hydrogels Composed of an Agarose/Poly(acrylamide-co-acrylic acid) Interpenetrating Network. *Macromol. Chem. Phys.* **2017**, *218*, No. 1700170.

(15) Li, X.; Wu, C.; Yang, Q.; Long, S.; Wu, C. Low-Velocity Superlubrication of Sodium-Alginate/Polyacrylamide Ionic-Covalent Hybrid Double-Network Hydrogels. *Soft Matter* **2015**, *11*, 3022−3033.

(16) Oogaki, S.; Kagata, G.; Kurokawa, T.; Kuroda, S.; Osada, Y.; Gong, J. P. Friction between Like-Charged Hydrogels—combined Mechanisms of Boundary, Hydrated and Elastohydrodynamic Lubrication. *Soft Matter* **2009**, *5*, 1879.

(17) Ou, K.; Dong, X.; Qin, C.; Ji, X.; He, J. Properties and Toughening Mechanisms of PVA/PAM Double-Network Hydrogels prepared by Freeze-Thawing and Anneal-Swelling. *Mater. Sci. Eng. C Mater. Biol. Appl.* **2017**, *77*, 1017−1026.

(18) Chen, Q.; Zhu, L.; Huang, L.; Chen, H.; Xu, K.; Tan, Y.; Wang, P.; Zheng, J. Fracture of the Physically Cross-Linked First Network in Hybrid Double Network Hydrogels. *Macromolecules* **2014**, *47*, 2140−2148.

(19) Zhang, Z.; Ye, Z.; Hu, F.; Wang, W.; Zhang, S.; Gao, L.; Lu, H. Double-Network Polyvinyl Alcohol Composite Hydrogel with Self-Healing and Low Friction. *J. Appl. Polym. Sci.* **2022**, *139*, 51563.

(20) Lin, T.; Bai, Q.; Peng, J.; Xu, L.; Li, J.; Zhai, M. One-Step Radiation Synthesis of Agarose/Polyacrylamide Double-Network Hydrogel with Extremely Excellent Mechanical Properties. *Carbohydr. Polym.* **2018**, *200*, 72−81.

(21) Shoaib, T.; Espinosa-Marzal, R. M. Advances in Understanding Hydrogel Lubrication. *Colloids Interfaces* **2020**, *4*, 54.

(22) Zhang, K.; Simic, R.; Yan, W.; Spencer, N. D. Creating an Interface: Rendering a Double-Network Hydrogel Lubricious via Spontaneous Delamination. *ACS Appl. Mater. Interfaces* **2019**, *11*, 25427−25435.

(23) Shoaib, T.; Prendergast, P.; Espinosa-Marzal, R. M. Compositional Tuning Reveals a Pathway to Achieve a Strong and Lubricious Double Network in Agarose-Polyacrylamide Hydrogels. *Tribol. Lett.* **2022**, *70*, 71.
(24) Rintoul, I.; Wandrey, C. Polymerization of Ionic Monomers in Polar Solvents: Kinetics and Mechanism of the Free Radical Copolymerization of Acrylamide/Acrylic Acid. *Polymer* **2005**, *46*, 4525−4532.
(25) Kim, J.; Zhang, G.; Shi, M.; Suo, Z. Fracture, Fatigue, and Friction of Polymers in which Entanglements Greatly Outnumber Cross-links. *Science* **2021**, *374*, 212−216.
(26) Anseth, K. S.; Bowman, C. N.; Brannon-Peppas, L. Mechanical Properties of Hydrogels and their Experimenta Determination. *Biomaterials* **1996**, *17*, 1647−1657.
(27) Ostroha, J.; Pong, M.; Lowman, A.; Dan, N. Controlling the Collapse/Swelling Transition in Charged Hydrogels. *Biomaterials* **2004**, *25*, 4345−4353.
(28) Renn, D. W. Agar and Agarose: Indispensable Partners in Biotechnology. *Ind. Eng. Chem. Prod. Res. Dev.* **1984**, *23*, 17−21.
(29) Pincus, P. Colloid Stabilization with Grafted Polyelectrolytes. *Macromolecules* **1991**, *24*, 2912−2919.
(30) Chung, K. H.; Lee, Y. H.; Kim, D. E. Characteristics of Fracture during the Approach Process and Wear Mechanism of a Silicon AFM tip. *Ultramicroscopy* **2005**, *102*, 161−171.
(31) Meyer, E. Site-Specific Friction Force Spectroscopy. *J. Vac. Sci. Technol. B: Microelectron. Nanometer Struct.* **1996**, *14*, 1285.
(32) Klein, J.; Kamiyama, Y.; Yoshizawa, H.; Israelachvili, J. N.; Fredrickson, G. H.; Pincus, P.; Fetters, L. J. Lubrication Forces between Surfaces Bearing Polymer Brushes. *Macromolecules* **1993**, *26*, 5552−5560.
(33) Klein, J.; Luckham, P. Forces between two Adsorbed Polyethylene Oxide Layers Immersed in a Good Aqueous Solvent. *Nature* **1982**, *300*, 429−431.
(34) Derjaguin, B. Molekulartheorie der äußeren Reibung. *Z. Phys.* **1934**, *88*, 661−675.
(35) Shoaib, T.; Heintz, J.; Lopez-Berganza, J. A.; Muro-Barrios, R.; Egner, S. A.; Espinosa-Marzal, R. M. Stick-Slip Friction Reveals Hydrogel Lubrication Mechanisms. *Langmuir* **2018**, *34*, 756−765.
(36) Pitenis, A. A.; Uruena, J. M.; Schulze, K. D.; Nixon, R. M.; Dunn, A. C.; Krick, B. A.; Sawyer, W. G.; Angelini, T. E. Polymer Fluctuation Lubrication in Hydrogel Gemini Interfaces. *Soft Matter* **2014**, *10*, 8955−8962.
(37) Shoaib, T.; Espinosa-Marzal, R. M. Insight into the Viscous and Adhesive Contributions to Hydrogel Friction. *Tribol. Lett.* **2018**, *66*, 96.
(38) Drummond, C. Electric-field-induced Friction Reduction and Control. *Phys. Rev. Lett.* **2012**, *109*, No. 154302.
(39) Chen, L.; Hu, W.; Du, M.; Song, Y.; Wu, Z.; Zheng, Q. Bioinspired, Recyclable, Stretchable Hydrogel with Boundary Ultralubrication. *ACS Appl. Mater. Interfaces* **2021**, *13*, 42240−42249.
(40) Zhang, H. J.; Sun, T. L.; Zhang, A. K.; Ikura, Y.; Nakajima, T.; Nonoyama, T.; Kurokawa, T.; Ito, O.; Ishitobi, H.; Gong, J. P. Tough Physical Double-Network Hydrogels Based on Amphiphilic Triblock Copolymers. *Adv. Mater.* **2016**, *28*, 4884−4890.
(41) Dong, M.; Han, Y.; Hao, X. P.; Yu, H. C.; Yin, J.; Du, M.; Zheng, Q.; Wu, Z. L. Digital Light Processing 3D Printing of Tough Supramolecular Hydrogels with Sophisticated Architectures as Impact-Absorption Elements. *Adv. Mater.* **2022**, *34*, No. e2204333.
(42) Bertsch, P.; Diba, M.; Mooney, D. J.; Leeuwenburgh, S. C. G. Self-Healing Injectable Hydrogels for Tissue Regeneration. *Chem. Rev.* **2023**, *123*, 834−873.
(43) Zhu, Y.; Li, X.; Zhao, Z.; Liang, Y.; Wang, L.; Liu, Y. Highly Stretchable, Transparent and Adhesive Ionogel Based on Chitosan-Poly(acrylic acid) Double Networks for Flexible Strain Sensors. *Gels* **2022**, *8*, 797.
(44) Means, A. K.; Ehrhardt, D. A.; Whitney, L. V.; Grunlan, M. A. Thermoresponsive Double Network Hydrogels with Exceptional Compressive Mechanical Properties. *Macromol. Rapid Commun.* **2017**, *38*, No. 1700351.
(45) Liu, J.; Liu, X.; Chen, J.; Wang, H.; Han, X.; Liu, H. Drying-Enhanced Polyvinyl Alcohol-Polyacrylic Acid Double-Network Hydrogel and its Application in Flexible Strain Sensors. *Chem. Eng. Sci.* **2022**, *264*, No. 118120.
(46) Chen, G.; Huang, J.; Gu, J.; Peng, S.; Xiang, X.; Chen, K.; Yang, X.; Guan, L.; Jiang, X.; Hou, L. Highly Tough Supramolecular Double Network Low-temperature Tolerant Sensor. *J. Mater. Chem. A* **2020**, *8*, 6776−6784.
(47) Deptula, A.; Wade, M.; Rogers, S. A.; Espinosa-Marzal, R. M. Charge-Induced Structural Changes of Confined Copolymer Hydrogels for Controlled Surface Morphology, Rheological Response, Adhesion, and Friction. *Adv. Funct. Mater.* **2022**, *32*, No. 2111414.
(48) Deptula, A.; Rangel-Galera, J.; Espinosa Marzal, R. M. Control of Surface Morphology, Adhesion and Friction of Colloidal Gels with Lamellar Surface Interactions. *Adv. Funct. Mater.* **2023**, No. 2300896.
(49) Sader, J. E.; Chon, J. W. M.; Mulvaney, P. Calibration of Rectangular Atomic Force Microscope Cantilevers. *Rev. Sci. Instrum.* **1999**, *70*, 3967−3969.
(50) Mullin, N.; Hobbs, J. K. A non-Contact, Thermal Noise based Method for the Calibration of Lateral Deflection Sensitivity in Atomic Force Microscopy. *Rev. Sci. Instrum.* **2014**, *85*, 113703.

https://doi.org/10.1021/acsami.3c00949
ACS Appl. Mater. Interfaces 2023, 15, 20495−20507